

ASSESSING THE COMBINED EFFECTS OF CHEMICAL AND MECHANICAL PARAMETERS ON SILAR-GROWN NANOSTRUCTURED ZnO THIN FILMS

BRAHIM YDIR^{1,3,*}, AMINE AJDOUR¹, MOUAD SOUMANE¹, SAMIA ACHOUCH²,
DRIS BEN HMAMOU¹, IULIA ANTOHE^{3,4,*}, GABRIEL SOCOL³,
LUIZA-IZABELA TODERAȘCU³, MARCELA SOCOL⁵, CĂTĂLIN LUCULESCU³,
RADOUANE LEGHRIB¹, HOUDA LAHLOU¹

¹Laboratory of Materials, Signals, Systems and Physical Modeling,
Faculty of Science, University Ibn Zohr-Agadir, Morocco

²Conception and Systems Laboratory, Mohammed V University in Rabat, Rabat, Morocco

³Laboratory of Lasers in Life Sciences, Environment and Manufacturing, National Institute for Lasers, Plasma and Radiation Physics, Atomistilor 409 Street, 077125 Magurele, Romania

⁴Academy of Romanian Scientists (AOSR), Ilfov 3 Street, 050044 Bucharest, Romania

⁵Laboratory of Optical Processes in Nanostructured Materials, National Institute of Materials Physics, Atomistilor 405A Street, 077125 Magurele, Romania

* Corresponding authors: iulia.antohe@inflpr.ro (IA); brahim.ydir@edu.uiz.ac.ma (BY)

Received May 27, 2024

Abstract. In the literature, a comprehensive assessment of the combined impacts of chemical and mechanical parameters on the properties of thin films grown by SILAR is missing. In this work, ZnO film formation is investigated under variable precursor concentration, pH, withdrawal speed and number of cycles. Interestingly, the produced ZnO films displayed remarkable aspect ratio and morphological variability, ranging from the commonly obtained nanograins shape towards hexagonal nanorods, flower-like rods and nanoneedles, which to our knowledge have not yet been achieved by using single step SILAR process. More particularly, low concentration and intermediate pH and withdrawal rates were favorable for nanorods formation. In addition, increasing the withdrawal speed from 26 to 30 cm·min⁻¹ resulted in a thinner film with improved rod uniformity and reduced crystallite size. This is the first study on the impact of substrate withdrawal speed on SILAR films. Among all studied parameters, the number of cycles was particularly useful for tuning film thickness, while preserving its target shape. In addition, the films grown under a higher number of cycles showed improved film crystallinity and rod orientation with reduced dislocation density, microstrain and bandgap energy. In our conditions, the most suitable combination of parameters required for exhibiting optimized nanorod-shaped coating are: a concentration of 0.07 M, pH of 10.5, speed of 30 cm·min⁻¹ and 40 cycles. In this case, XRD, XPS, Raman and FTIR spectra displayed typical features of hexagonal Wurtzite structure of ZnO with no impurities within the film surface, whereas AFM measured a thickness of 1.4 μm with 243 nm surface roughness.

Key words: ZnO, thin film, SILAR, nanograins, nanoneedles, nanoflowers, nanorods, concentration, pH, withdrawal speed, number of growth cycles.

DOI: <https://doi.org/10.59277/RomRepPhys.2024.76.508>

1. INTRODUCTION

The technology advanced significantly in the last decade, providing faster, more efficient and smaller electronic devices [1–3]. Semiconductor thin film technology is part of many cutting-edge tools, such as transparent electronics, sensor manufacturing, photovoltaics, sensing, etc. [4, 5]. Among the wide family of semiconductor materials, zinc oxide (ZnO) is renowned for matching some distinctive advantages, such as high optical transparency, high electron mobility, wide bandgap, good piezoelectric properties and chemical stability, making it so attractive as an active material for developing a wide range of semiconductor devices [6–9]. In addition, ZnO is generally considered a low-cost, safe, non-toxic and non-carcinogenic material. It is also a biodegradable material that does not accumulate in the environment [10, 11]. ZnO can exist in different phases, such as the wurtzite, zinc blende and cubic rocksalt structures, depending on the chosen synthesis method and treatment conditions. Among these phases, the former remains the most stable phase in normal conditions of temperature and pressure [12–14]. ZnO thin films are more commonly shaped as interconnected particles, with diameters in the nanometer range, generally less than 100 nm. However, thanks to the recent advances in nanotechnology, ZnO nanostructured thin films are also available in diverse forms, such as nanorods with a nanometric diameter and length or can take the form of 2D structures such as nanosheets of nanometric thickness and extended lateral dimensions, among others. These sheets can be plate- or flake-shaped [15]. Controlling and understanding the shape and composition of ZnO is necessary to tailor its functional properties towards the requirements of specific applications, such as photocatalysis, solar cells, sensors and energy storage devices, and improve the overall device performance [16].

Up-to-date, ZnO nanostructured thin films can be processed by using different physical or chemical deposition methods, depending on the desired properties and applications. Most deposition techniques adopt four main steps: (1) substrate preparation, (2) material deposition, (3) post-deposition treatment, and (4) characterization. The second step, deposition, can be done using several techniques, such as Chemical Bath Deposition (CBD) [17–20], Atomic Layer Deposition (ALD) [21–23], Chemical Vapor Deposition (CVD) [24], Electro-Deposition (ED), Spray Pyrolysis (SP) [25], and Successive Ionic Layer Adsorption and Reaction (SILAR) [26–35], to name a few. CBD involves a controlled chemical reaction to create a thin layer through a heterogeneous deposition. ALD is a derivation of CVD based on alternating precursors under a controlled vacuum to obtain a homogeneous and highly ordered film on the substrate, in contrast to CVD, which uses high temperatures and a continuous flow of precursor chemicals onto the substrate. ED is a technique based on a potentiostatic controller with three electrodes and with temperature and pH control instruments. This latter is preferable for conductive substrates. SP is an approach for thin film deposition by spraying a solution over a heated surface, where the constituents react to create a chemical composite. More particularly, SILAR is a

deposition technique used to fabricate thin films or coatings with precise control over thickness and composition. SILAR involves the sequential deposition of precursor solutions onto a substrate, followed by reaction and adsorption steps. The process begins by immersing the substrate in a solution containing a precursor of one of the desired film constituents (for example ZnO). The substrate is then washed and dried to remove any excess solution. This cycle is repeated multiple times, with each cycle depositing a single atomic or molecular layer onto the substrate. The key advantage of SILAR is its simplicity and low cost compared to other deposition techniques. It can be performed at room temperature and atmospheric pressure, making it suitable for a wide range of substrates and applications [26–32]. Also, SILAR technique combines some unique advantages of ALD and CBD. In fact, SILAR deposition takes a physically distinct layer-by-layer process like ALD, with CBD flexibility using atmospheric coating from aqueous metal salt solutions, in the absence of high vacuum equipment. As illustrated in Table 1, the main difference between these techniques centers on six points, such as the equipment, film thickness and coating conditions, substrate selectivity, deposited layer quality and cost [36–38].

SILAR process involves several parameters, including choice and concentration of precursor solution, substrate temperature, pH, immersion time, withdrawal speed and number of growth cycles [36, 37]. In literature, the effect of precursor solution concentration has been widely studied on the properties of ZnO thin films grown by using different chemical techniques [39–47]. The results of these studies have concretely demonstrated the notable effect of concentration on the development of different morphologies of ZnO films [6]. This latter has usually increased in crystal size, microstrain, defect density and film thickness [40–46]. However, in the case of ZnO films grown by SILAR, the concentration effect was only reported once [40]. In this work, the increase of precursor solution molarity from 0.025 M to 0.125 M was shown to induce an improvement in film crystallinity, without any observed change in the nanograin morphology. Also, in chemical methods, pH is usually considered another critical parameter that affects the surface and structural properties of ZnO thin films [48–54]. The increase in solution pH has been accompanied by an increase in crystal size and film thickness and a reduction of film transparency [48–51, 54], in contrast to the results obtained in [53]. However, most of these studies did not address sufficiently the pH selection criteria. In some cases, the obtained thin films suffered from low crystal quality and homogeneity [48, 52, 53]. To the best of our knowledge, only one work in the literature has dealt with the effect of pH on ZnO thin film formation by SILAR. The crystallite size and film thickness were found to increase as a result of pH increase from 8.5 to 10.5. Also, the films demonstrated a change from grain morphology at 8.5, to flower-like structures at 9.0, and to a mixture of grains and rods at 9.5 and finally to elongated rods sticking with each other at 10.5. However, in this case, the films showed no explicit morphology due to their non-uniform nature. This limitation could be due to the study of the pH effect as a single variable, and not together with the other SILAR variables, such as

concentration. Concerning the effect of mechanical parameters, the number of cycles is one of the critical parameters that has been reported in [55–60], but in the case of ZnO thin films, this has only been studied once by Ydir and co-workers [61]. In this work, the increase in the number of growth cycles induced an increase in film grain sizes and thickness and a decrease in optical bandgap. Nevertheless, other mechanical parameters, such as substrate withdrawal speed, have not yet been investigated, although their effect on the film thickness and uniformity of the SILAR-deposited films is highly expected. Consequently, it is imperative to optimize the withdrawal speed of a particular SILAR process in order to achieve the desired properties of the synthesized film.

In addition, it's still worth mentioning that the dominant morphology in the literature for SILAR-deposited thin films is the nanograin morphology. Obtaining other morphologies, with higher aspect ratios, has usually required combining the SILAR technique with other processes. In this sense, Taha and co-workers produced ZnO thin films by using a two-step process, in which the seed layer was grown by SILAR, followed by CBD. The authors found that the final morphologies of ZnO thin films were dependent on the CBD growth duration. The films grown for 6 h displayed mixed nanorods/nanodisks shapes, whereas those grown for 10 and 12 h showed nanodisks-like morphology [62]. Also, Kumar and co-authors, found that the selection of seed layers (deposited by SILAR) was very crucial for obtaining highly ordered and good quality of ZnO nanostructures grown by CBD. Moreover, the growth and orientation of the produced ZnO nanostructures were tailored by tuning the morphology of the seed layer. Accordingly, the spherical-shaped and dart-like morphology of the ZnO seed layers resulted in the growth of ZnO nanorods and nanospines, respectively [63]. Nevertheless, such two-step processes complicate the deposition process, extend the deposition time and induce an increase in precursor and chemical agent consumption. Also, despite the significant results achieved by SILAR, the reported studies on thin films still suffer from some limitations, which can be summarized in two points: Firstly, most reported studies only focus on the independent effect of a single parameter as an independent variable and do not include the chemical and mechanical combination, which is crucial to optimize the film growth process. Also, no works in the literature have addressed the effect of withdrawal speed on thin film properties deposited by SILAR. Secondly, in the particular case of ZnO thin films, there is a lack of an in-depth characterization of the effect of concentration, pH and number of growth cycles, as only one work has been reported on each parameter. All these limitations explain why the produced morphology is generally limited to the shape of nanograins.

To fill in this gap, the novelty of this work consists of exploring, for the first time in literature, the formation of ZnO thin film by SILAR under the combination of chemical (concentration and pH) and mechanical (withdrawal speed and number of cycles) parameters, by using a home-made automated equipment. The first aim is to explore the possibilities offered by this technique in terms of morphological and

structural variability, which are supported by SEM, EDS, XRD and UV-visible spectroscopy analysis. The second aim is to identify, for the first time, the suitable combination of parameters for obtaining well-aligned nanorods film morphology based on a single step SILAR process. In this case, an in-depth characterization is conducted by AFM, FT-IR, XPS, and RAMAN spectroscopy to evaluate the optimized film topography, thickness and composition.

Table 1
Comparison of various thin-film deposition techniques [36–38]

	CBD	ALD	CVD	ED	SP	SILAR
Equipment	Simple aqueous bath with controlled temperature	Cost-effective gas distribution system & vacuum chamber	Gas distribution system & vacuum and high temperature	Potentiostatic system equipped with three electrodes, with temperature and pH control instruments	Pyrolysis spray coating unit comprising a vacuum, an injector and a heated surface	Simple coating
Thickness Control	Practical control of solution temperature and concentration down to the micrometer scale.	Practically difficult high thicknesses with perfect control	Practically difficult high thicknesses with very good control	Thickness depends on the application with very good control	Practical control using solution viscosity, temperature and injection velocity	Practical control using the solution concentration and cycle numbers' down to the low micrometer scale
Coating conditions	Ambient temperature and pressure	Vacuum conditions and moderate temperature	Reduced pressure and high-temperature	Controlled temperature, pH, and potential	High and moderate temperature with a heated surface	Ambient temperature and pressure
Substrate selectivity	Wide range of substrates	Wide range of substrates	Limited by deposition temperature	Conductive substrate	Substrate resisting to moderate and high temperatures	Wide range of substrates
Deposited film Quality	Depends on experimental parameters	Excellent	Excellent	High quality	Depends on coating environment	Depends on experimental parameters
Cost	Low	High	High	Low	Low	Low

SILAR: Successive Ionic Layer Adsorption and Reaction; **CBD:** Chemical Bath Deposition; **ALD:** Atomic Layer Deposition; **CVD:** Chemical Vapor Deposition; **ED:** Electro-Deposition; **SP:** Spray Pyrolysis.

2. EXPERIMENTAL SETUP

Figure 1 presents a schematic illustration of the homemade automated SILAR equipment used in this study to grow ZnO thin films [26]. This latter is composed of three main components, namely: the motorized platform the electronic control circuit, and the visual user interface. As displayed in Fig. 1a, the moving platform,

equipped with a 4-substrate holder, enables precisely controlling the substrate movement and position, both along the x-axis and across the y-axis, by using stepper motors. The electrical control circuit depicted in Fig. 1b, allows the programming, processing, and execution of various operating instructions for actuators, sensors, and other devices. Examples include power sources, stepper motor drivers, etc. It permits customizing each component's power supply. Finally, the graphical interface shown in Fig. 1c, allows customizing and easily adjusting the SILAR deposition parameters, namely: number of beakers to be used, immersion time in each beaker, the distance separating the beakers (Δd), the substrate immersion depth (d_y), the immersion/withdrawal speed along the X and Y-axis and the number of growth cycles. More details on the design and the electromechanical features of the equipment are available elsewhere [23].

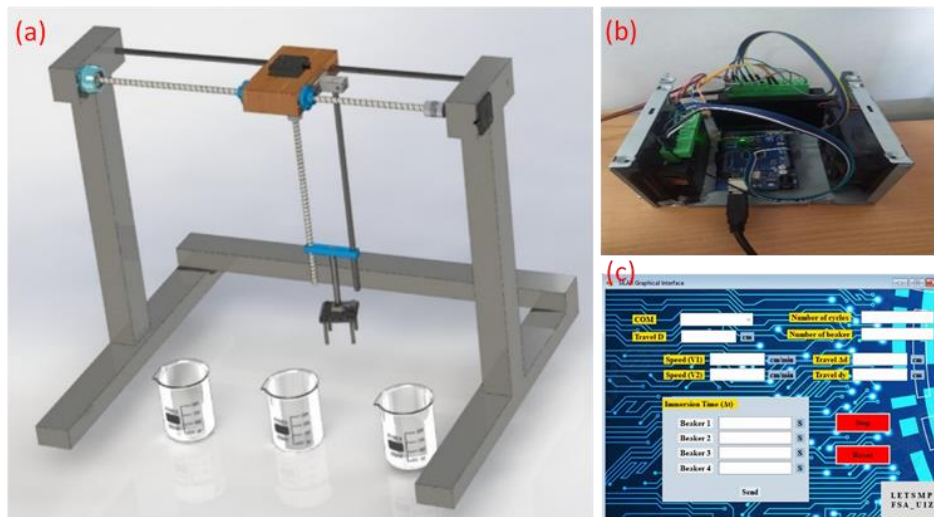


Fig. 1 – a) Home-made automated equipment used to grow thin films by SILAR; b) Electronic control circuit; (c) User control interface [23].

3. FILM GROWTH PROCEDURE

3.1. SILAR PROTOCOL

The deposition trials of ZnO thin films were performed on glass substrates using the automated SILAR equipment. Before deposition began, the substrates were cleaned inside an ultrasonic bath, in five successive steps, containing: deionized water, acetone, and deionized water again, then ethanol, and finally deionized water. Each step lasts for 15 minutes. Subsequently, the substrates were dried before use. Note that all the chemical reagents used to clean the substrates (acetone, ethanol,

etc.), as well as the zinc chloride ($ZnCl_2$) precursor and ammonia used to produce the different films of ZnO, were of analytical grade and purchased from Sigma Aldrich. The reaction precursors were prepared with distilled water having a resistance of less than $2\text{ M}\Omega\cdot\text{cm}$.

Figure 2 depicts a schematic description of the SILAR process. For the synthesis of ZnO thin films, the cationic solution was prepared by mixing distilled water with precisely measured proportions of $ZnCl_2$ and ammonia (NH_3). In this study $ZnCl_2$ was selected among other precursors, based on its several advantages reported elsewhere [64]. Then, the obtained mixture was magnetically stirred at room temperature for one hour to get a uniform and transparent solution.

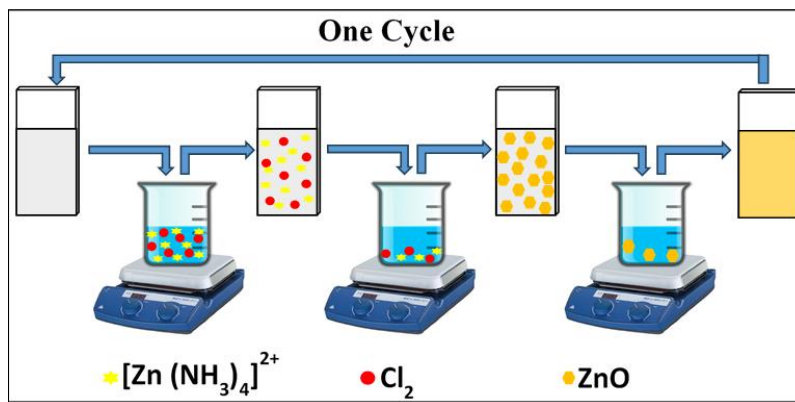


Fig. 2 – Schematic representation of the SILAR process.

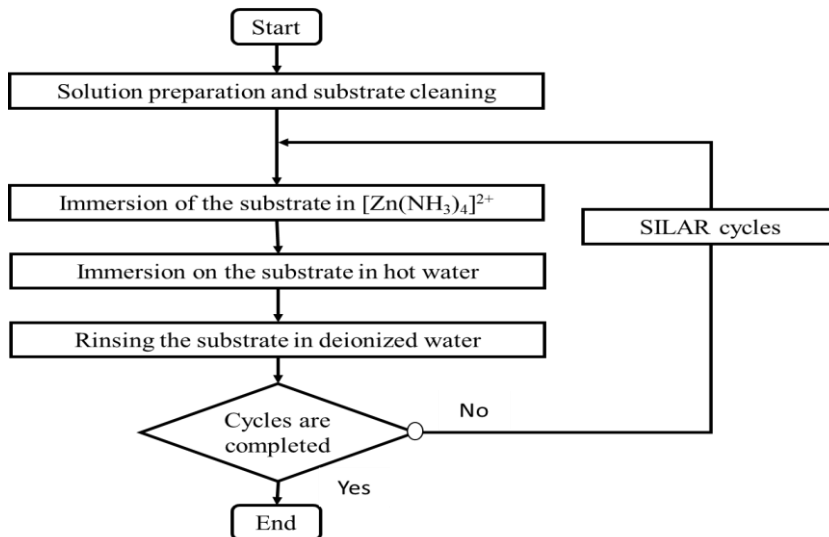


Fig. 3 – Flowchart of ZnO film deposition by the SILAR method.

ZnO thin films were deposited by alternating the substrate dipping in $[\text{Zn}(\text{NH}_3)_4]^{2+}$ complex and heated water. Each single immersion cycle consisted of the following three stages:

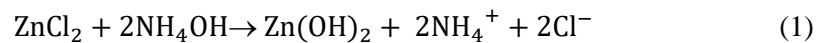
- (1) *immersion of the substrate in the cationic solution to absorb the complex onto the substrate;*
- (2) *submersion the substrate in hot water to obtain a solid layer of ZnO;*
- (3) *washing of the substrate with a sufficient amount of distilled water to eliminate unreacted species in advance to the next deposition cycle.*

Figure 3 depicts the flowchart of ZnO film deposition by the SILAR method. Therefore, numerous immersions are required for obtaining compact, homogeneous and well-adhered ZnO thin films and achieving the target thickness.

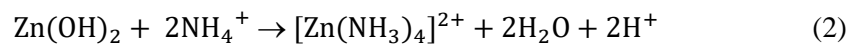
3.2. FILM GROWTH PRINCIPLE

The formation of ZnO thin films onto a glass substrate by using the SILAR technique required the use of two separated cationic and anionic solutions. Ammonia acts as a complexing agent and serves to control bath pH. The first bath consisted of a ZnCl_2 solution; in which, the zinc (II) tetra ammonium complex $[\text{Zn}(\text{NH}_3)_4]^{2+}$ is shaped by the excessive addition of ammonia [65].

In the first SILAR step, zinc ions are complexed by the hydroxide $[\text{Zn}(\text{NH}_3)_4]^{2+}$ and get adsorbed onto the substrate surface. During the adsorption, the zinc-hydroxide complex is eventually partially broken up. After rinsing, in the reaction step, hydrogen peroxide and hydroxide ions from the anion precursor solution adsorb onto the surface and react with the adsorbed zinc species. Equation 1 depicts the saponification reaction when aqueous ammonia is added to the ZnCl_2 solution. The ammonia addition causes the Zn^{2+} ions to interact with the OH^- ion to generate a white precipitate of $\text{Zn}(\text{OH})_2$.

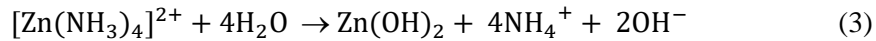


Excess NH_4OH is added to dissolve the hydroxide, resulting in a clear solution of two different chemical species, as shown in Eq. 2.



When the glass substrate is immersed in the aforementioned solution, the zinc complex ions are adsorbed onto the substrate due to the attraction forces between the ions in the solution and the surface of the substrate. These forces can be Van der Waals, cohesive, or chemical attraction [28]. The glass substrate is then immersed in

hot water, and the $[\text{Zn}(\text{NH}_3)_4]^{2+}$ complex decomposes to yield $\text{Zn}(\text{OH})_2$ according to Eq. 3:



Equation 4 shows the dehydration reaction that occurs at the substrate surface leading to the formation of ZnO from an ammonium zincate bath:



Thus, the successful formation of a well-adhering and homogeneous ZnO film on the substrate occurs within a suitable number of cycles. Among the most important experimental parameters influencing the deposition and film quality process are the molar ratio of $\text{Zn}/\text{NH}_4\text{OH}$, the time duration of the reaction in hot water, and the drying process.

3.3. PROCESSING PARAMETERS

Table 2 describes the different chemical and mechanical SILAR parameters tested in our deposition trials. Concerning chemical parameters, we started by examining the concentration effect. During these experiments, different films were deposited by changing the precursor concentration (ZnCl_2) in the cationic solution, while keeping the pH value at 10.5, the withdrawal speed at $30 \text{ cm}\cdot\text{min}^{-1}$, and the number of growth cycles at 40. The variation of the metallic content of the films was obtained by preparing the precursor at different molarities in deionized water. Each solution was prepared with a specific concentration by measuring the corresponding amount before being dissolved in 50 mL of distilled water. In order to evaluate the effect of pH, different films were prepared by varying the pH value of the precursor solution, while keeping the ZnCl_2 salt concentration constant at 0.07 M, the withdrawal speed at $26 \text{ cm}\cdot\text{min}^{-1}$ and the number of growth cycles to 40, during all experiments. The solution pH was adjusted to different values by using ammonia, namely: 10, 10.5 and 11. Concerning the mechanical parameters, the study of the effect of substrate withdrawal rate, by using our homemade automated machine, was performed by setting the motor speed along the y-axis to three different values, namely: $20 \text{ cm}\cdot\text{min}^{-1}$; $30 \text{ cm}\cdot\text{min}^{-1}$ and $45 \text{ cm}\cdot\text{min}^{-1}$. Meanwhile, solution concentration and solution pH were fixed at their optimal values of 0.07 M and 10.5, respectively. To determine the number of growth cycle's effect, ZnO solutions were prepared using optimal precursor concentration, pH and withdrawal speed of $30 \text{ cm}\cdot\text{min}^{-1}$. The film deposition was carried out under a variable number of cycles of: 10, 20, 30 and 40, to yield ZnO semiconductor thin films of various thicknesses. All the experiments were conducted at room conditions. After deposition, the different samples were heat-treated in a muffle furnace at 400°C for 1 hour, to eliminate residual solvents and allow the crystallization of ZnO.

Table 2

Studied chemical and mechanical SILAR parameters: Description, parameter labels and values

	Deposition Parameter	Description	Label and Value
Chemical	Precursor Concentration (mol. L ⁻¹)	Means the amount of precursor present in a given volume of cationic solution	C1 = 0.07 C2 = 0.085 C3 = 0.1 C4 = 0.13
	pH	Is a measure of the chemical activity of protons or hydrogen ions in the cationic solution	P1 = 10 P2 = 10.5 P3 = 11
Mechanical	Withdrawal speed (cm·min ⁻¹)	The rate at which the substrate is dipped into the solution and withdrawn from it during the deposition process	S1 = 20 S2 = 30 S3 = 45
	Number of cycles	The number of times the substrate is exposed to alternating solutions containing cations and anions	N1 = 10 N2 = 20 N3 = 30 N4 = 40

4. ZnO FILM FORMATION UNDER VARIABLE SILAR PARAMETERS

Investigation of ZnO film formation under combined effects of chemical and mechanical SILAR parameters was carried out by Scanning Electron Microscopy (SEM) and Energy Dispersive X-ray spectroscopy (EDX), by using JEOL model JSM-6700F equipment. X-ray diffraction (XRD) patterns were acquired by a Bruker D8 advanced diffractometer under Cu K α irradiation ($\lambda = 1.54060 \text{ \AA}$), whereas film bandgap energy was characterized by UV-Vis spectroscopy.

4.1. EFFECT OF CHEMICAL PARAMETERS

A. PRECURSOR CONCENTRATION

Figure 4 shows SEM images of the ZnO thin films manufactured at variable precursor concentrations of 0.07 mol/L, 0.085 mol/L, 0.1 mol/L and 0.13 mol/L. As a first observation, all films were homogeneous, compact and well bonded onto the glass substrate. Moreover, we didn't notice any macroscopic defects such as voids, pinholes, or spalling on the deposited film surface which might induce the occurrence of photocurrent leakage, in accordance with [66, 67]. The film grown at a concentration of C1 = 0.07 mol/L displayed hexagonal-shaped nanorods. However, by increasing the solution concentration to C2 = 0.085 mol/L, a flower-like morphology was observed, as a result of random nanorod agglomeration. In addition, a change from flower-like morphology to grain morphology was observed at C3 = 0.1 mol/L. Then, agglomerated nanograins were detected above

the latter concentration (case of $C4 = 0.13 \text{ mol/L}$), in line with [68, 69]. Figure 4e presents the EDS analysis performed on the sample prepared at a concentration of 0.07 mol/L (hexagonal-shaped nanorods). This analysis validated the existence of the Zn and O elements in ZnO, with no significant impurities or contamination. We can also notice the absence of peaks related to other components, such as Si and Ca, associated with the glass substrate, thanks to the uniform, homogeneous and compact layer, obtained under 40 cycles [27]. These results demonstrate the possibility of tuning film surface morphology by playing with precursor solution concentration and outperform other studies, where the nanograin morphology of ZnO film was maintained regardless of precursor concentration [40].

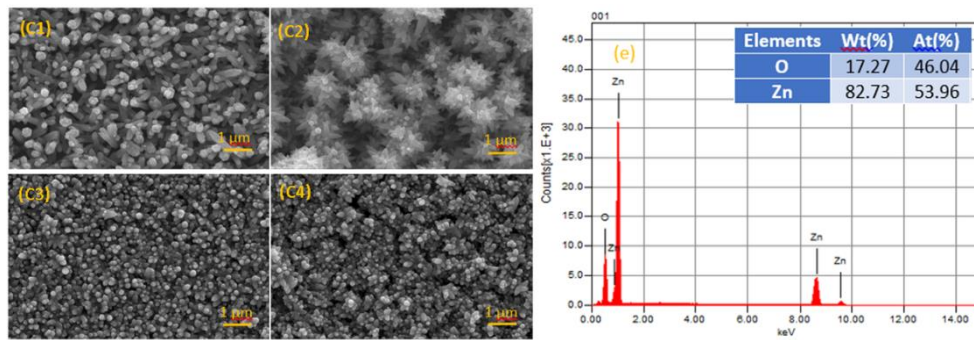


Fig. 4 – SEM images of the ZnO thin films prepared under variable solution concentrations of: C1 = 0.07 mol/L , C2 = 0.085 mol/L , C3 = 0.1 mol/L and C4 = 0.13 mol/L
(e) EDX spectra of ZnO deposited at a concentration of 0.07 mol/L .

B. SOLUTION PH

Figure 5 presents the XRD spectra of ZnO films obtained under three solution pH values, namely: 10, 10.5 and 11. All diffractograms were coherent with the standard database of Crystallography: JCPDS: 36-1451, revealing the formation of the hexagonal polycrystalline Wurtzite structure with a preferable growth along the (002) plane. Also, it is noticeable that the peak intensities increased with pH, indicating an improvement in the degree of crystallinity of ZnO, as shown by the first three peaks of the (100) (002) and (101) planes [70]. Table 3 completes Fig. 5, by summarizing the Full-Width at Half Maximum (FWHM), interplanetary distance (d), and crystallite size values of the different samples. Hence, as the pH increased, the FWHM decreased, revealing an increase in average crystal size. It's not worth mentioning that the crystallite size (D) was determined from the full width at half maximum (FWHM) of the scattered diffraction patterns via Scherrer's formula [71]:

$$D = \frac{0.9\lambda}{\beta \cos(\theta)} \quad (1)$$

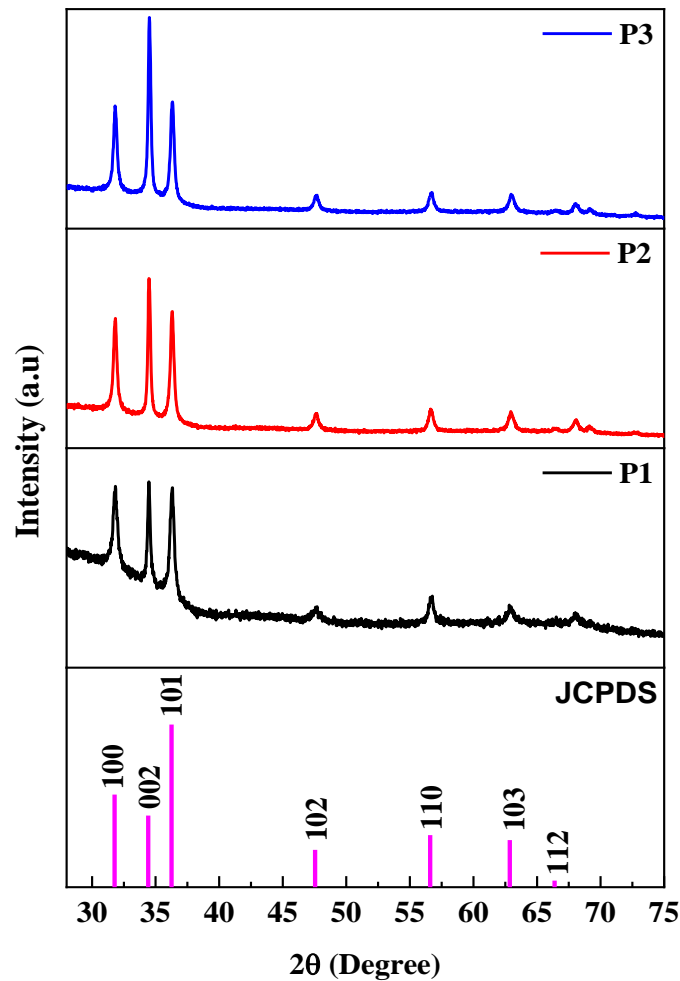


Fig. 5 – XRD spectra of ZnO thin-films prepared at various pH values.

SEM images of Fig. 6, reveal the formation of a massive and continuous coating. Three morphologies can be identified among the deposited films, namely: granular for P1, nanorods with some grain traces for P2 and randomly oriented needles- or feather-shaped nanorods for P3. In the lower pH range, with weak OH^- ions, $\text{Zn}(\text{OH})_2$ can form with the released OH^- ions, allowing the deposition of a coating of finely spherical particles. On the contrary, for higher pH baths, the density of OH^- ions is significantly higher. The OH^- present at higher pH and the released OH^- promote the continued growth of $\text{Zn}(\text{OH})_2$ in the cationic bath, which transforms partially into full-sized nanorods, as observed in the case of P2 sample. Then, above a certain pH value, the samples are converted to randomly oriented needle-like morphology [72, 73, 74]. This means that intermediate pH (10.5) may favor the formation of vertically oriented rods, as is the case for P2 sample, which should

minimize surface roughness and benefit for optical properties, conversely to the P1 and P3 micrographs. Sathivelu and co-workers [70] have reported a similar tendency. However, the ZnO coatings produced in our case, exhibited an improved uniformity, which can be further enhanced by optimizing the mechanical parameters [75].

Table 3

Summary of the structural parameters of the ZnO films deposited at various pH values

pH	2θ (°)	hkl	d (Å)	FWHM (β)	Lattice parameters (Å)	Crystallite size D(nm)	Microstrain ε (× 10 ⁻⁴) lines ⁻² m ⁻⁴	Dislocation density δ (× 10 ⁺¹⁴) lines m ⁻²
P1 = 10	31.84	1 0 0	0.2808	0.42	a = 3.2423664 c = 5.1904777	21.12	32.4	22.4
	34.53	0 0 2	0.2595	0.32				
	36.33	1 0 1	0.2471	0.44				
P2 = 10.5	31.86	1 0 0	0.2807	0.36	a = 3.2408971 c = 5.1870744	24.57	27.6	16.6
	34.56	0 0 2	0.2594	0.28				
	36.33	1 0 1	0.238	0.36				
P3 = 11	31.84	1 0 0	0.2808	0.31	a = 3.2429229 c = 5.1989986	28.99	23.6	11.9
	34.47	0 0 2	0.2599	0.23				
	36.31	1 0 1	0.2472	0.31				

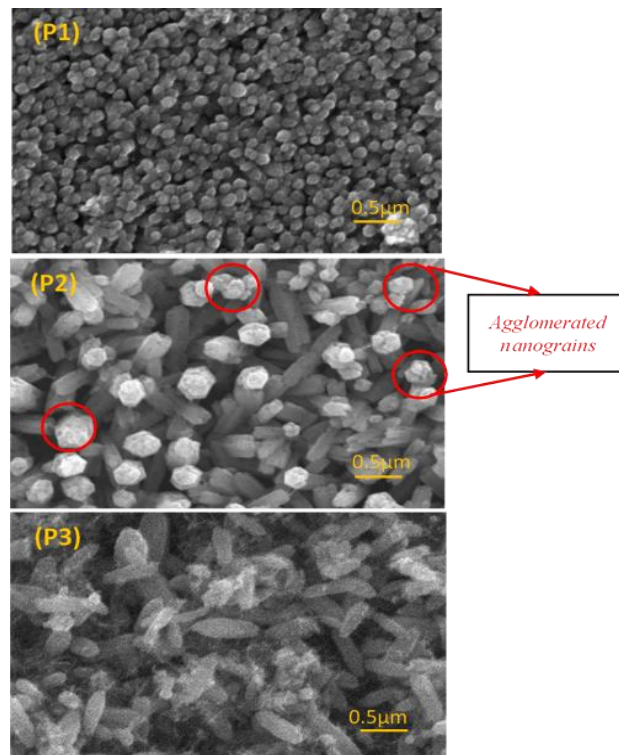


Fig. 6 – SEM images of the ZnO films obtained using various pH values: P1 = 10, P2 = 10.5 and P3 = 11.

4.2. MECHANICAL PARAMETERS

After exploring the effect of chemical parameters and identifying the precursor concentration and pH values required to obtain nanorod morphology, namely: C1 and P2. The study can be complemented by investigating the effect of the mechanical parameters, namely withdrawal speed and the number of growth cycles. These two complementary parameters will help to strengthen the validity of the previously obtained results and provide stronger recommendations. Also, they can provide additional and in-depth information on the performance, reliability and applicability of the approaches used in this study.

A. WITHDRAWAL SPEED

Figure 7 shows XRD diagrams for the films grown at three withdrawal speeds: $S1 = 20 \text{ cm}\cdot\text{min}^{-1}$, $S2 = 30 \text{ cm}\cdot\text{min}^{-1}$ and $S3 = 45 \text{ cm}\cdot\text{min}^{-1}$. The diffraction peaks are in agreement with the Joint Committee on Powder Diffraction Standards (JCPDS) diagram reference number 36-1451. From the nature of the three dominant peaks at 31.84° , 34.53° , and 36.33° , corresponding to the (100), (002), and (101) planes, we can affirm the polycrystalline nature of the ZnO films. All the samples show a single phase, justified by the absence of Bragg peaks corresponding to other phases. Also, crystallite size is reduced with increased withdrawal speed, accompanied by an enhancement in the degree of crystallinity and an increase in dislocation density as illustrated in Table 4.

Figure 8 shows SEM micrographs of the films obtained at the three withdrawal speeds, namely: S1, S2, and S3. The morphologies identified are nanograins for S1, nanorods for S2, and flower-based nanorods for S3. ImageJ software estimated three average grain sizes: 143 nm for S1, 115 nm for S2 and 90 nm for S3. This grain size evolution is consistent with the crystallite size obtained from XRD analysis. More particularly, the film grown under S2 ($30 \text{ cm}\cdot\text{min}^{-1}$) presents more uniform nanorods perpendicular to the substrate surface, thereby further improving the quality of the morphology identified in P2 (pH = 10.5 under $26 \text{ cm}\cdot\text{min}^{-1}$). Then, we can deduce that the P2 and S2 combination makes it possible to exhibit ZnO coating with an explicit nanorod morphology, which has not yet been observed in the literature.

After examining the withdrawal speed's effect on structural and surface properties, we will focus on its influence on optical properties. For this reason, the sample absorbance spectra of the different films are shown in Fig. 9. The bandgap energy values were calculated using thickness values obtained from ZnO transmittance spectra (using the two envelopes method) and the Tauc curve method.

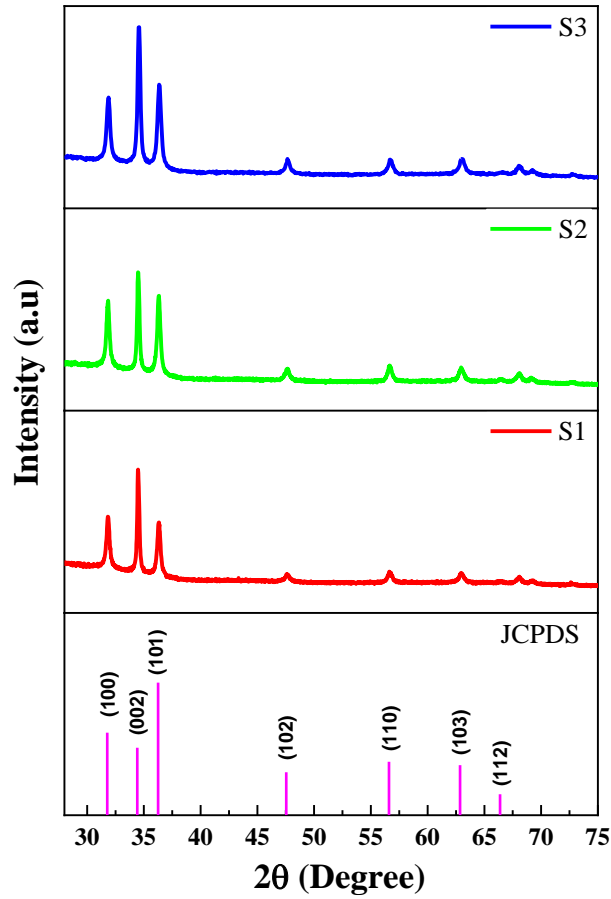


Fig. 7 – XRD patterns of ZnO thin films prepared under variable withdrawal speed

Table 4

Calculated structural parameters of the films prepared under variable withdrawal speed

Withdrawal speed (cm·min ⁻¹)	2θ	hkl	d (Å)	FWHM (β)	Lattice parameters (Å)	Crystallite size D (nm)	Dislocation density δ (× 10 ⁺¹⁴ lines m ⁻²)
S1 = 20	31.83	1 0 0	0.2809	0.3229	a = 3.2436	25.37	15.53
	34.48	0 0 2	0.2598	0.21024	c = 5.1871		
	36.32	1 0 1	0.2471	0.3155			
S2 = 30	31.85	1 0 0	0.2807	0.2807	a = 3.2416	24.43	16.75
	34.48	0 0 2	0.2597	0.2598	c = 5.1971		
	36.32	1 0 1	0.247	0.2471			
S3 = 45	31.88	1 0 0	0.281	0.3474	a = 3.2382	22.3	20.11
	34.58	0 0 2	0.2598	0.2759	c = 5.1923		
	36.34	1 0 1	0.2472	0.368			

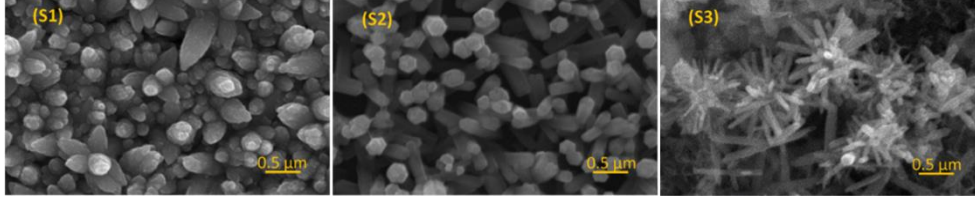


Fig. 8 – SEM images of the ZnO thin films prepared using different withdrawal speeds of: (S1) 20 cm·min⁻¹, (S2) 30 cm·min⁻¹, and (S3) 45 cm·min⁻¹

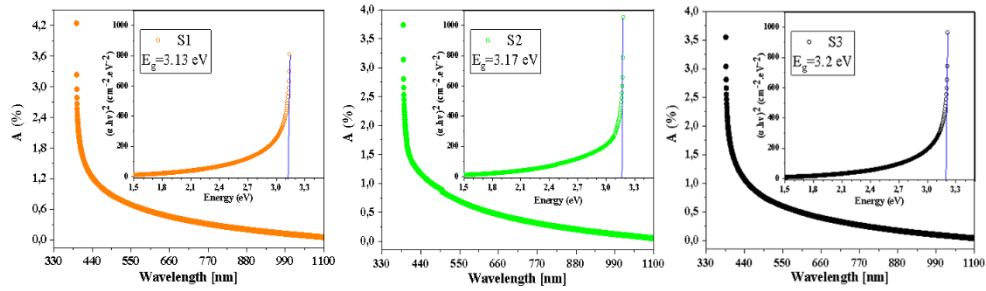


Fig. 9 – Absorbance spectra and plots of $(\alpha h\nu)^2$ versus $(h\nu)$ for ZnO thin films prepared at various withdrawal speeds S1, S2, and S3.

The absorption factor (α) is determined for all samples according to the formula below [76]:

$$\alpha = \frac{1}{t} \cdot \ln\left(\frac{1}{T}\right) \quad (\text{II})$$

where t and T represent film thickness and transmittance ratio, respectively.

The relationship between optical bandgap and absorption coefficient (α) is detailed as follows [77]:

$$\alpha h\nu = B(h\nu - E_g)^m \quad (\text{III})$$

where α is the material absorption coefficient, B is an energy-independent constant, $h\nu$ is the photon energy, and m is a strength coefficient determining the optical transition type ($m = 1/2$ for direct transition).

Direct bandgap energies of 3.13 eV, 3.17 eV, and 3.2 eV were obtained for S1, S2, and S3 samples, respectively. The observed increase in film bandgap energy is in accordance with the redshift observed in the absorption edge. The decrease in absorbance can be attributed to the decrease of film thickness, due to crystallite and grain size reduction, as a result of the increase of withdrawal speed, as confirmed by XRD and

SEM results. To the best of our knowledge, this is the first study examining the withdrawal speeds effect on the properties of thin films deposited by the SILAR method.

B. NUMBER OF GROWTH CYCLES

Figure 10 shows SEM images for N1, N2, N3, and N4 samples. The concentration (C1), pH (P2), and withdrawal speed (S2) enabled us to maintain the nanorod morphology, whereas the number of cycles affected thickness. Also, it's noticeable from Fig. 10 that the film produced under 10 cycles showed randomly oriented nanorods whose orientation enhanced progressively as far as the number of cycles increased. At 40 cycles, the film exhibited the best nanorod alignment along the vertical axis.

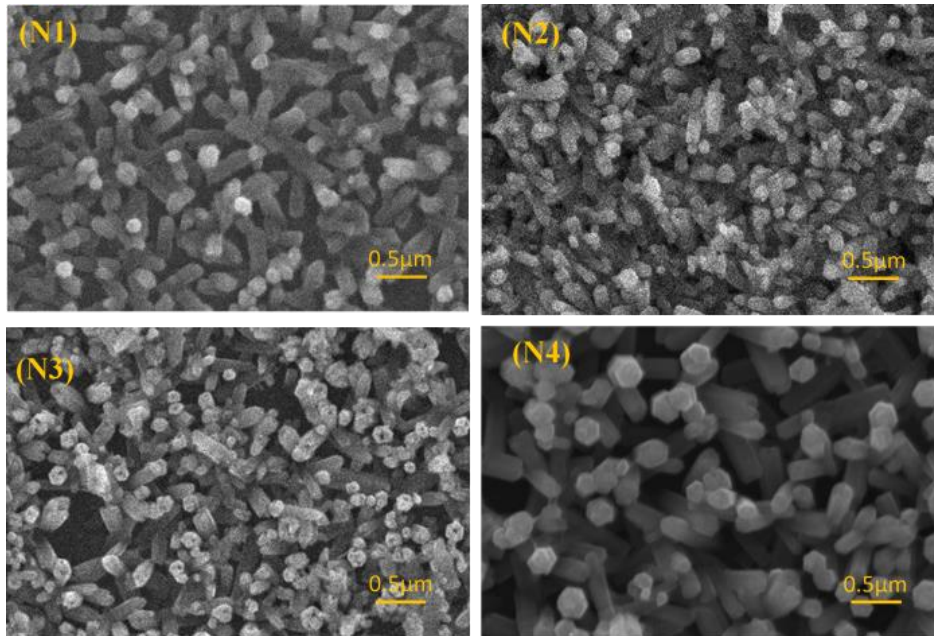


Fig. 10 – SEM images of the ZnO thin films prepared under variable number of cycles: N1 = 10, N2 = 20, N3 = 30, and N4 = 40.

Figure 11 presents XRD patterns for the samples produced under N1 = 10, N2 = 20, N3 = 30, and N4 = 40. The polycrystalline structure of the films is always preserved. Furthermore, the structural parameters in Table 5 indicate a clear improvement of the crystal structure and a reduction of dislocation density and micro-strain, with the increase of the number of cycles [57]. These results are consistent with other studies [55, 78].

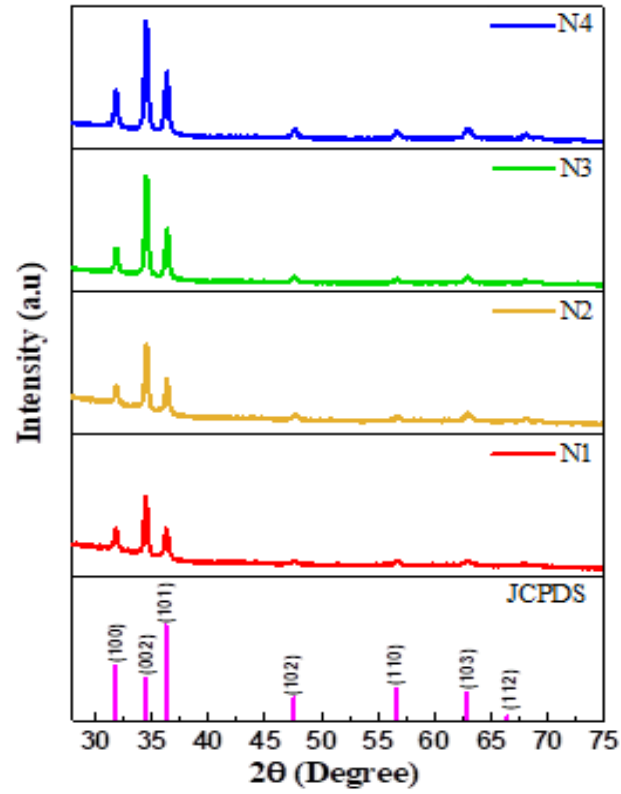


Fig. 11 – XRD patterns of ZnO films prepared under variable number of cycles: 10, 20, 30, and 40.

Table 5

Calculated structural parameters of the films prepared under different number of cycles

Number of growth cycles	2θ (°)	hkl	d (Å)	FWHM (β)	Lattice parameters (Å)	Crystallite size D (nm)	Dislocation density δ ($\times 10^{+14}$ lines m^{-2})
N1	31,83	1 0 0	0,281	0,31694	a = 3,2407 c = 5,192305	21,19	22,2
	34,5	0 0 2	0,259	0,31715			
	36,32	1 0 1	0,247	0,35431			
N2	31,82	1 0 0	0,281	0,332	a = 3,2447 c = 5,2011	22,5	19,6
	34,46	0 0 2	0,259	0,2967			
	36,29	1 0 1	0,247	0,3224			
N3	31,85	1 0 0	0,280	0,30327	a = 3,24174 c = 5,1923	23,77	17,7
	34,52	0 0 2	0,259	0,2711			
	36,35	1 0 1	0,247	0,34006			
N4	31,82	1 0 0	0,281	0,29923	a = 3,244 c = 5,18107	26,04	14,7
	34,46	0 0 2	0,260	0,29788			
	36,29	1 0 1	0,247	0,3561			

Figure 12 depicts the absorbance spectra and tauc plots of the different samples. The bandgap energies for samples N1, N2, N3, and N4 were 3.5, 3.34, 3.25, and 3.15 eV, respectively in accordance with the observed blueshift of the absorption edge. The observed decrease of the bandgap as a function of the number of cycles is attributed to the decrease in transmittance, meaning the increase in film thickness [26]. The explanation for the bandgap of 3.5 eV for N1 can be attributed to the quantum size effect predicted by the monocrystalline nature caused by the small size of the crystals [21]. This finding is important compared to other studies [79, 80]. Among all studied SILAR parameters, the number of growth cycles, was the unique parameter, which allowed tuning film thickness while keeping the target surface morphology.

Therefore, the sample produced at 40 cycles has a relatively larger crystal size and lower dislocation density with a good nanorod shape and a better alignment, thereby reducing the grain boundaries effect compared to the other previously observed morphologies (grains, flowers, needles, etc.). These properties remain particularly attractive for photo-electrodes, solar cells, and gas detection applications.

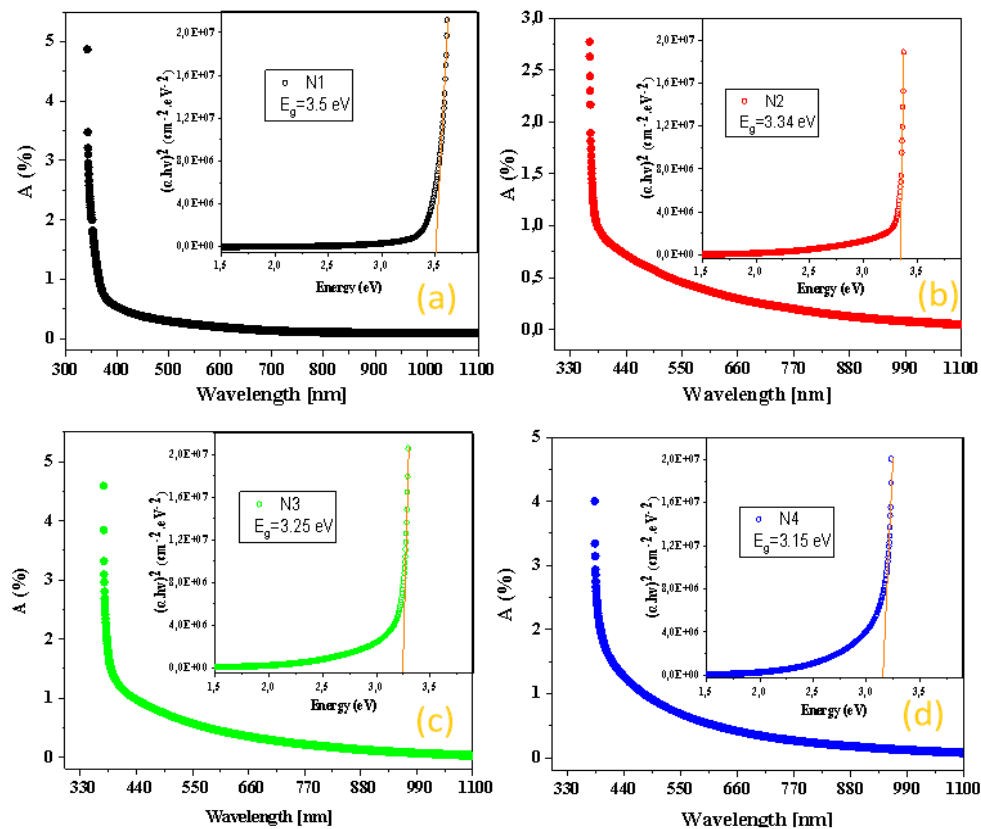


Fig. 12 – Absorbance spectra and plots of $(\alpha h\nu)^2$ versus $(h\nu)$ for ZnO thin films prepared under different number of cycles (a) 10, (b) 20, (c) 30, and (d) 40.

4.3. NANOROD-FILM TOPOGRAPHY AND COMPOSITION

In the previous section, we successfully identified the parameters required for exhibiting nanorod morphology, namely: C1 for concentration, P2 for pH, S2 for withdrawal speed, and N4 for the number of cycles. These selections are justified by our aim to obtain an aligned nanorod morphology (C1, P2) and an explicit hexagonal wurtzite structure with fully controlled thickness (S2, N4). The topography and composition of the exhibited thin film properties are further investigated.

On one hand, Atomic Force Microscopy (AFM) in tapping mode was used to examine the topography of the nanorod-shaped film by using a Nanonics MV 4000 Microscope over a scan area of $10\ \mu\text{m} \times 10\ \mu\text{m}$. On another hand, film surface composition was examined by Fourier Transform Infrared (FTIR) X-ray Photoelectron Spectroscopy (XPS) and Raman spectroscopy, using PerkinElmer FTIR spectrometer (PerkinElmer, Inc., MA, USA), ESCALAB Xi+ (Thermo SCIENTIFIC Surface Analysis) equipped with a multichannel hemispherical electron analyzer (dual X-ray source) working with Al $K\alpha$ radiation ($h\nu = 1486.2\ \text{eV}$) and a BRUKER-RFS27 FT-Raman spectrometer (Bruker Optik GmbH, Bremen, Germany), respectively.

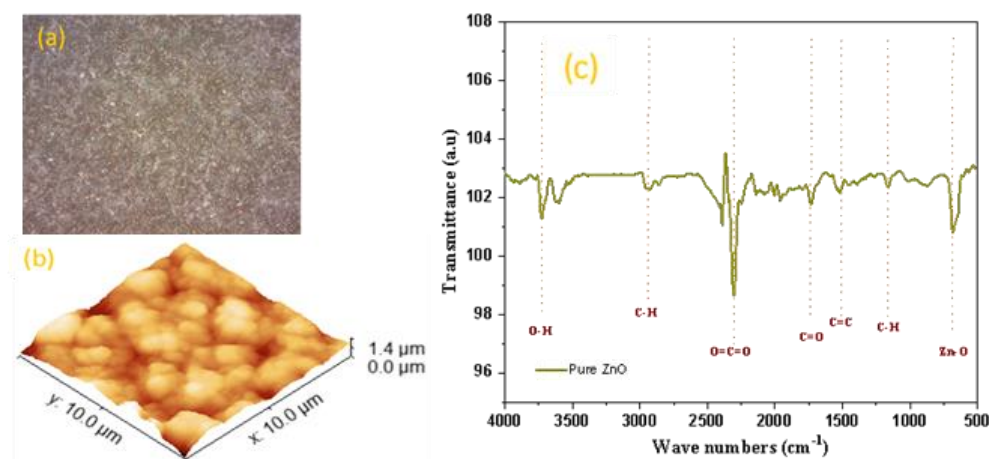


Fig. 13 – (a, b) Atomic force microscopic view of the ZnO film surface (c) FTIR spectrum of the film.

Figure 13 (a and b) shows Atomic Force Microscopy (AFM) images of the surface of the nanorod-shaped ZnO film. Accordingly, the film exhibited an average thickness of $1.4\ \mu\text{m}$ and an average surface Root Mean Square (RMS) roughness of $243\ \text{nm}$. Figure 13c depicts the FTIR spectrum, which provides information on chemical bonding and composition on the film surface of pristine ZnO. The vibration band at $3906\ \text{cm}^{-1}$ could be attributed to the hydroxyl group (OH). The peak at $2305\ \text{cm}^{-1}$ represents the CO_2 molecule in the air, whereas the bands detected at 2929 and $1158\ \text{cm}^{-1}$ can be attributed to C-H bonding. The band detected at $667\ \text{cm}^{-1}$ corresponds to Zn-O stretching, which confirms ZnO formation.

XPS analysis was used to understand the chemical state, electronic structure and film composition. Figure 14a shows the XPS spectra of the film, with Zn, O, and C as the main constituents. The spectrum of Zn 2p, displayed in Fig. 14b, shows two bands at 1045.0 and 1021.5 eV, corresponding to Zn 2p_{1/2} and Zn 2p_{3/2} electronic states, respectively. The gap between the Zn 2p_{3/2} and Zn 2p_{1/2} electronic states was calculated to be 23.0 eV. This is generated by spin-orbit splitting and is identical to previously reported values [81]. As shown in Fig. 14c, the O1s XPS peak can be decomposed into two Gaussian components at ~531.4 and 530 eV; the band at 530.0 eV can be indexed to chemisorbed oxygen species at the sample surface and lattice oxygen vacancies (O_C), whereas the band at 531.4 eV can be indexed to lattice oxygen species (O_L) in the Wurtzite structure of hexagonal ZnO.

Figure 14d shows the Raman spectrum of ZnO film, measured under 532 nm excitation. The vibration mode at ~450 cm⁻¹ is attributed to the second-order Raman mode (E_{2H}) associated with oxygen atoms, a typical feature of hexagonal wurtzite ZnO [82]. Peaks around 560 and 785 cm⁻¹ generally result from second-order Raman scattering, although the presence of impurities and/or defects may also influence these modes. The mode observed at 932 cm⁻¹ is attributed to the A₁ polar mode corresponding to the vibration of the C-C bond. The additional mode at 1100 cm⁻¹ observed in the Raman spectrum of ZnO is attributed to surface optical phonon modes [83].

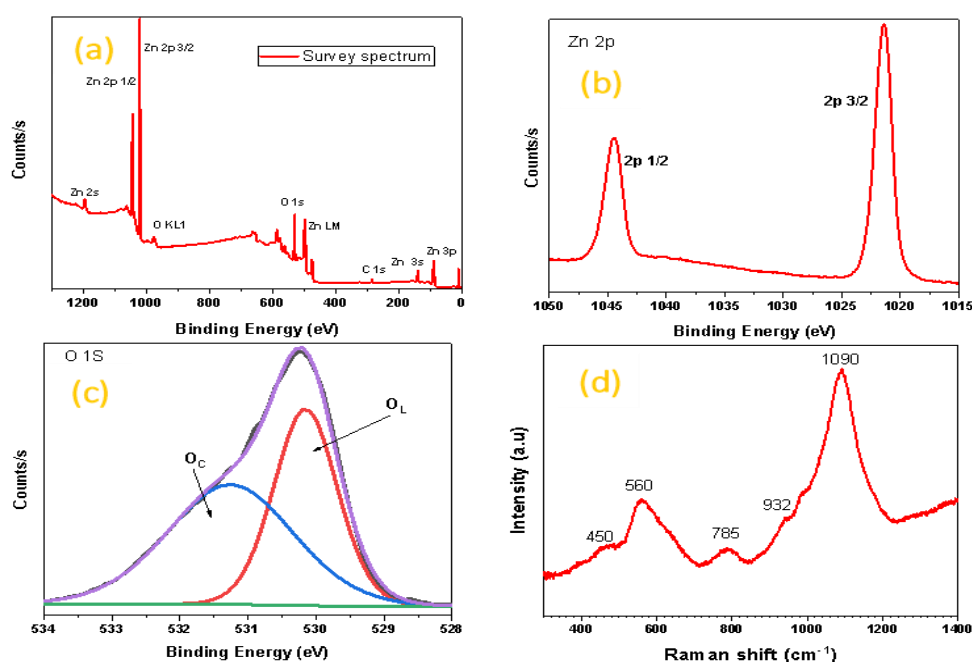


Fig. 14 – a) XPS survey spectra of ZnO nanorod-film; b) Zn 2p_{1/2} and 2p_{3/2} core level scans; c) XPS core level scan of O 1s; d) Raman spectra of ZnO.

5. CONCLUSIONS

This work investigated for the first time the formation of ZnO thin films by single-step SILAR process under the combination of two important types of parameters, namely chemical and mechanical ones. Thanks to the use of our homemade automated SILAR equipment, it was possible to customize and perform the growth process under variable mechanical parameters such as substrate withdrawal speed and number of growth cycles, in addition to the chemical parameters such as precursor concentration and pH in the cationic solution. Regardless of the growth conditions, all produced ZnO films annealed at 400°C, exhibited a unique hexagonal wurtzite phase with no detected impurities. Nevertheless, thanks to the combination of concentration, pH and withdrawal speed, it was possible to extend, for the first time the variability of the shapes of ZnO films produced by one-step SILAR to nanorods, flower-like rods and nanoneedles, rather than the nanograin shape usually observed using this technique. More particularly, low concentration together with intermediate pH and withdrawal rates in the range of 26-30 cm·min⁻¹ were favorable for nanorod formation. In addition, by increasing withdrawal speed from 26 to 30 cm·min⁻¹ thinner films were obtained with improved rod uniformity and reduced crystallite size. Hence, it should be mentioned, that this is the first study on the impact of substrate withdrawal speed on SILAR films. In contrast to the three aforementioned variables, the number of cycles was the lonely parameter, which allowed preserving film shape, while allowing to tune the film thickness. In particular, the film grown under a higher number of cycles showed improved film crystallinity and rod orientation with reduced dislocation density, microstrain and bandgap energy. In our conditions, the suitable combination of parameters required for exhibiting optimized nanorod-shaped coating was identified as follows: a concentration of 0.07 M, pH of 10.5, speed of 30 cm·min⁻¹ and 40 cycles. In such conditions, the nanorod-shaped film displayed a thickness of 1.4 μm with a Root Mean Square surface roughness of 243 nm. The parametric approach adopted in this study pointed out for the first time the necessity to involve the mechanical parameters especially withdrawal rate in combination with the other parameters when designing and optimizing semiconductor thin films for a specific application and opens the way for the fabrication of ZnO films with tunable shapes and functional properties, taking the advantages of the affordability and simplicity of the SILAR process, whose main produced morphology was usually limited to nanograins. Future work will involve (1) extending our investigation by involving the impact of other parameters, namely immersion angle and annealing temperature, and (2) validating the optimal parameters in the mark of a gas sensing application.

Acknowledgements. This work was supported by a doctoral scholarship program "Eugen Ionescu" 2023 through the Ministry of Foreign Affairs, by the National Authority for Research and Innovation in the framework of the Nucleus Programme – LAPLAS VII (grant 30N/2023) and by a grant of the Ministry of Research, Innovation and Digitalization, CNCS/CCCDI-UEFISCDI, project

number ERANET-M-3-GasSensingMat-RT-1, within PNCDI IV. B.Y. acknowledges the Romanian Ministry of Foreign Affairs and the Agence Universitaire de la Francophonie (AUF) for the Eugen Ionescu research and mobility grant at the National Institute for Laser, Plasma and Radiation Physics (INFLPR). I.A. acknowledges the Academy of Romanian Scientists (AOSR) via the AOSR-TEAMS 2023-2024 project.

REFERENCES

1. J. Rudolph, S. Tan, and S. Tan, *ChatGPT: Bullshit spewer or the end of traditional assessments in higher education*, *J. Appl. Learn. Teach.* **6**, 342–363 (2023).
2. M. Zhang, S. Liu, Z. Wang, Y. Yuan, Z. Zhang, Q. Liang, X. Yang, Z. Duan, Y. Liu, F. Kong, B. Liu, B. Ren, and Z. Tian, *Progress in soybean functional genomics over the past decade*, *Plant Biotechnology Journal* **20**, 256–282 (2022).
3. F. Gustafsson, and J.G. Rogers, *Left ventricular assist device therapy in advanced heart failure: patient selection and outcomes*, *Eur. J. Heart Fail.* **19**, 595–602 (2017).
4. M. Mikulics, J. Mayer, and H.H. Hardtdegen, *Cutting-edge nano-LED technology*, *J. Appl. Phys.* **131**, 110903 (2022).
5. H.R. Han, *Hybrid Fiber Materials according to the Manufacturing Technology Methods and IOT Materials: A Systematic Review*, *Materials* **16**, 1351 (2023).
6. R. Woods-Robinson, Y. Han, H. Zhang, T. Ablekim, I. Khan, K.A. Persson, and A. Zakutayev, *Wide band gap chalcogenide semiconductors*, *Chem. Rev.* **120**, 4007–4055 (2020).
7. S. Vyas, *A short review on properties and applications of zinc oxide based thin films and devices: ZnO as a promising material for applications in electronics, optoelectronics, biomedical and sensors*, *Johnson Matthey Technol. Rev.* **64**, 202–218 (2020).
8. M.A. Borysiewicz, *ZnO as a functional material, a review*, *Crystals* **9**, 505 (2019).
9. O. Gençyılmaz, I. Akyüz, and F. Atay, *Binary ZnS–ZnO films as an alternative buffer layer for solar cell applications*, *Appl. Phys. A Mater. Sci. Process.* **130**, 227 (2024).
10. D.K. Sharma, S. Shukla, K.K. Sharma, and V. Kumar, *A review on ZnO: Fundamental properties and applications*, *Mater. Today Proc.* **49**, 3028–3035 (2022).
11. A.D. Terna, E.E. Elemike, J.I. Mbonu, O.E. Osafire, and R.O. Ezeani, *The future of semiconductors nanoparticles: Synthesis, properties and applications*, *Mater. Sci. Eng. B Solid-State Mater. Adv. Technol.* **272**, 115363 (2021).
12. R. Munprom, C. Sae-Tiaw, S. Phiankoh, O. Jongprateep, K. Surawathanawises, and R. Techapiesancharoenkij, *Structural, optical, and electrical modification of hydrothermally grown ZnO nanorods by tin-doping*, *Mater. Res. Express* **6**, 095916 (2019).
13. F.H. Abdullah, N.H.H.A. Bakar, and M.A. Bakar, *Current advancements on the fabrication, modification, and industrial application of zinc oxide as photocatalyst in the removal of organic and inorganic contaminants in aquatic systems*, *J. Hazard. Mater.* **424**, 127416 (2022).
14. S. Mansy, H. Musleh, S. Shaat, J. Asad, and N. AlDahoudi, *Computational and experimental study of wurtzite phase ZnO nanoparticles*, *Mater. Today Commun.* **35**, 105688 (2023).
15. Z. Arshad, S. Shakir, A.H. Khoja, A.H. Javed, M. Anwar, A. Rehman, R. Javaid, U.Y. Qazi, and S. Farrukh, *Performance Analysis of Calcium-Doped Titania (TiO₂) as an Effective Electron Transport Layer (ETL) for Perovskite Solar Cells*, *Energies* **15**, 1408 (2022).
16. K. Wang, M. Janczarek, Z. Wei, T. Raja-Mogan, M. Endo-Kimura, T.M. Khedr, B. Ohtani, and E. Kowalska, *Morphology and crystalline composition-governed activity of titania-based photocatalysts: Overview and perspective*, *Catalysts* **9**, 1054 (2019).
17. A.F. Abdulrahman, N.M. Abd-Alghafour, and S.M. Ahmed, *Optimization and characterization of SILAR synthesized ZnO nanorods for UV photodetector sensor*, *Sensors Actuators A Phys.* **323**, 112656 (2021).

18. S. Kumar, R. Seth, S. Panwar, K.K. Goyal, V. Kumar, and R.K. Choubey, *Morphological and Optical Studies of ZnO-Silica Nanocomposite Thin Films Synthesized by Time Dependent CBD*, *J. Electron. Mater.* **50**, 3462–3470 (2021).
19. N. Navya, K.K. Ribin, and K. Naseema, *Effect of post irradiation of IR light on the structural, morphological and optical properties of ZnO thin film grown by CBD method*, *Materials Today: Proceedings* **42**, 475–478 (2020).
20. H. Wang, S. Dong, Y. Chang, X. Zhou, and X. Hu, *Microstructures and photocatalytic properties of porous ZnO films synthesized by chemical bath deposition method*, *Appl. Surf. Sci.* **258**, 4288–4293 (2012).
21. C. Zhang, Q. Tu, L.F. Francis, and U.R. Kortshagen, *Band Gap Tuning of Films of Undoped ZnO Nanocrystals by Removal of Surface Groups*, *Nanomaterials* **12**, 565 (2022).
22. H. Kim, M.J. Jung, M.H. Lee, and B.J. Choi, *ALD growth of ZnO on GaN: Schottky barrier height engineering using ZnO interlayer*, *Mater. Today Commun.* **33**, 104434 (2022).
23. H. Kim, M.J. Jung, S. Choi, and B.J. Choi, *ALD growth of ZnO on p-Si and electrical characterization of ZnO/p-Si heterojunctions*, *Mater. Today Commun.* **25**, 101265 (2020).
24. V.K. Kaushik, C. Mukherjee, T. Ganguli, and P.K. Sen, *Electrical and optical characteristics of aerosol assisted CVD grown ZnO based thin film diode and transistor*, *J. Alloys Compd.* **696**, 727–735 (2017).
25. S. Roguai and A. Djelloul, *A structural and optical properties of Cu-doped ZnO films prepared by spray pyrolysis*, *Appl. Phys. A Mater. Sci. Process.* **126**, 122 (2020).
26. B. Ydir, A. Nidhāj, O. Bouaaliouat, Y. Ait-Wahmane, K. Bouabid, A. El Fanaoui, A. Ihlal, M. Bousseta, and H. Lahlou, *Towards the development of a gas micro-sensor based on nano-structured zinc oxide thin film for ethanol gas detection*, *Mater. Today Proc.* **52**, 89–94 (2021).
27. B. Ydir, D. Ben, H. Youssef, A. Wahmane, A. Ihlal, M. Bousseta, and H. Lahlou, *Electrodeposition, E.D. Design, implementation, and characterization of an automated SILAR system: validation with ZnO thin film deposition*, *Int. J. Adv. Manuf. Technol.* **123**, 1189-1201 (2022).
28. M.R. Alfaro Cruz, R. Garza-Hernández, P.P. Horley, J. Mata-Ramírez, E. Martínez-G., and F.S. Aguirre-Tostado, *Low temperature ZnO films grown by successive ionic layer adsorption and reaction method*, *Thin Solid Films* **663**, 49–55 (2018).
29. K.R. Devi, G. Selvan, M. Karunakaran, K. Kasirajan, L.B. Chandrasekar, M. Shkir, and S. AlFaify, *SILAR-coated Mg-doped ZnO thin films for ammonia vapor sensing applications*, *J. Mater. Sci. Mater. Electron.* **31**, 10186–10195 (2020).
30. S. Majumder, N.D. Quang, T.T. Hien, N.D. Chinh, N.M. Hung, H. Yang, C. Kim, and D. Kim, *Effect of SILAR-anchored ZnFe₂O₄ on the BiVO₄ nanostructure: An attempt towards enhancing photoelectrochemical water splitting*, *Appl. Surf. Sci.* **546**, 149033 (2021).
31. S. Sutha, S.C. Vanithakumari, R.P. George, U.K. Mudali, B. Raj, and K.R. Ravi, *Studies on the influence of surface morphology of ZnO nail beds on easy roll off of water droplets*, *Appl. Surf. Sci.* **347**, 839–848 (2015).
32. S.C. Shei, P.Y. Lee, and S.J. Chang, *Effect of temperature on the deposition of ZnO thin films by successive ionic layer adsorption and reaction*, *Appl. Surf. Sci.* **258**, 8109–8116 (2012).
33. Ş. Çavdar, Y. Şahin, N. Turan, H. Koralay, and N. Tuğluoğlu, *Structural and electrical characterization of Cd-doped ZnO thin films produced on p-type Si substrate by SILAR technique*, *J. Mater. Sci. Mater. Electron.* **34**, 1787 (2023).
34. I. Jellal, O. Daoudi, K. Nouneh, M. Boutamart, S. Briche, G. Plantard, M. Fahoume, and J. Naja, *Successive ionic layer adsorption and reaction (SILAR) synthesis of micro-structured Cu-doped ZnO thin films with enhanced photocatalytic activity*, *J. Mater. Sci. Mater. Electron.* **34**, 672 (2023).
35. I. Karaduman Er, M.A. Yıldırım, H.H. Örkücü, A. Ateş, and S. Acar, *Structural, morphological and gas sensing properties of Zn_{1-x}Sn_xO thin films by SILAR method*, *Appl. Phys. A Mater. Sci. Process.* **127**, 230 (2021).

36. M.A.M. Patwary, *Thin Films Processed by SILAR Method, In Thin Films-Deposition Methods and Applications - IntechOpen* (2022).
37. H. Soonmin, *Recent Advances in the Growth and Characterizations of SILAR-Deposited Thin Films*, Appl. Sci. **12**, 8184 (2022).
38. S.P. Ratnayake, J. Ren, E. Colusso, M. Guglielmi, A. Martucci, and E. Della Gaspera, *SILAR Deposition of Metal Oxide Nanostructured Films*, Small **17**, 2101666 (2021).
39. M. Khan, M. H. Irfan, M. Israr, N. Rehman, T.J. Park, and M.A. Basit, *Comparative investigation of ZnO morphologies for optimal CdS quantum dot deposition via pseudo-SILAR method*, Chemical Physics Letters **744**, 137223 (2020).
40. A.S. Amalraj, and G. Senguttuvan, *Effect of Solution Molarity on the Structural, Morphological and Optical Properties of Nanostructured Zinc Oxide Thin Films*, Journal of Chemical and Pharmaceutical Sciences **10**, 867–870 (2017).
41. V.A. Owoeye, E. Ajenifuja, A.E. Adeoye, A.O. Salau, S.A. Adewinbi, A.T. Akindadelo, D.A. Pelemo, and A.P.I. Popoola, *Effect of precursor concentration on corrosion resistance and microstructure of ZnO thin films using spray pyrolysis method*, Sci. African **15**, e01073 (2022).
42. D.T. Speaks, *Effect of concentration, aging, and annealing on sol gel ZnO and Al-doped ZnO thin films*, Int. J. Mech. Mater. Eng. **15**, 2 (2020).
43. R. Amari, A. Mahroug, A. Boukhari, B. Deghfel, and N. Selmi, *Structural, Optical and Luminescence Properties of ZnO Thin Films Prepared by Sol-Gel Spin-Coating Method: Effect of Precursor Concentration*, Chinese Phys. Lett. **35**, 016801 (2017).
44. A. Ayana, F. Hou, J. Seidel, B.V. Ranjendra, and P. Sharma, *Microstructural and piezoelectric properties of ZnO films*, Mater. Sci. Semicond. Process. **146**, 106680 (2022).
45. S. Murugesan, R. Shankararajan, K. Savarimuthu, K. Ramany, G. Rajamanickam, S. Narendhiran, and R. Perumalsamy, *Effect of Precursor Concentration on Structural, Morphological, and Optical Properties of ZnO Thin-Filmed Sensor for Ethanol Detection*, IEEE Trans. Nanotechnol. **17**, 169–176 (2018).
46. T. Ma, *Effect of precursor concentration and sintering on functional properties of ZnO thin films deposited by aerosol-assisted chemical vapour deposition (AACVD)*, Mater. Sci. Semicond. Process. **121**, 105413 (2021).
47. E. Nurfani, M.P. Ali, A. Rianjanu, L. Nulhakim, M.S. Anrokhi, and G.T.M. Kadja, *Effect of solution molarity on the optical and photocatalytic properties of sprayed ZnO film*, Mater. Chem. Phys. **309**, 128412 (2023).
48. O. Coskun, C.T. Altaf, M. Sankir, and N.D. Sankir, *ZnO-nanoflower thin film photoanodes for photoelectrochemical water splitting: Effect of pH and gallium doping*, Mater. Lett. **325**, 132900 (2022).
49. P.U. Londhe, and N.B. Chaure, *Effect of pH on the properties of electrochemically prepared ZnO thin films*, Mater. Sci. Semicond. Process. **60**, 5–15 (2017).
50. M.N. Murthy, C.J. Sreelatha, G. Ravinder, and S. Anusha, *The effect of solution pH on the structural, surface morphological, and optical characteristics of ZnO thin films synthesized by the chemical bath deposition technique*, Mater. Today Proc. **54**, 602–607 (2022).
51. J.C. Babu and V. Jagadeesan, *Impact of pH on the structural characteristics of spin coated zinc oxide thin films*, Mater. Today Proc. **66**, 2226–2229 (2022).
52. A. Zaidi, K. Tiwari, R.R. Awasthi, and K.C. Dubey, *Effect of pH values on the structural, morphological and sensing properties of ZnO nanostructure*, Chalcogenide Lett. **20**, 33–41 (2023).
53. S. Kumar, H.C. Jeon, T.W. Kang, R. Seth, S. Panwar, S.K. Shinde, D.P. Waghmode, R.G. Saratale, and R.K. Choubey, *Variation in chemical bath pH and the corresponding precursor concentration for optimizing the optical, structural and morphological properties of ZnO thin films*, J. Mater. Sci. Mater. Electron. **30**, 17747–17758 (2019).
54. L. Al-Farsi, T.M. Souier, M. Al-Hinai, M.T.Z. Myint, H.H. Kyaw, H.M. Widatallah, and M. Al-Abri, *pH Controlled Nanostructure and Optical Properties of ZnO and Al-Doped ZnO Nanorod Arrays Grown by Microwave-Assisted Hydrothermal Method*, Nanomaterials **12**, 3735 (2022).

55. O. Erken, *Effect of cycle numbers on the structural, linear and nonlinear optical properties in Fe₂O₃ thin films deposited by SILAR method*, *Curr. Appl. Phys.* **34**, 7–18 (2022).
56. M. Albayrak, O. Kiyak, and H. Güney, *Oda Sıcaklığında SILAR Tekniği İle Üretilen CdO Filmlerinin Kalınlık Farkının Optik Özellikleri Ve Yapısal Morfolojik Üzerindeki Etkisi*, *Erzincan University Journal of Science and Technology* **15**, 19–29 (2022).
57. N.J. Egwunyenga, V.C. Onuabuchi, N.L. Okoli, and I.E. Nwankwo, *Effect of SILAR Cycles on the Thickness, Structural, Optical Properties of Cobalt Selenide Thin Films*, *Int. Res. J. Multidiscip. Technovation* **3**, 1–9 (2021).
58. P.M. Geethanjali, K. Deepa, and T.L. Remadevi, *Effect of number of cycles on SILAR deposited ZnSe thin films*, *AIP Conf. Proc.* **2352**, 020011 (2021).
59. Z.A. Hamid, H.B. Hassan, M.A. Hassan, M.H. Mourad, and S. Anwar, *Deposition, characterization, performance of cadmium sulfide quantum dots thin films using SILAR technique for quantum dot sensitized solar cell applications*, *Key Eng. Mater.* **835**, 374–383 (2020).
60. K.O. Ighodal, T.M. Emeakaroha, B.N. Ezealigo, and K. Iloure, *Influence of Dip Cycles on the Structural, Optical and Morphological Properties of CdS-SILAR Deposited Thin Films*, *Journal of NanoScience, NanoEngineering and Applications* **6**, 19–26 (2016).
61. B. Ydir, D. Ben, H. Youssef, A. Wahmane, A. Ihlal, M. Bousseta, and H. Lahlou, *Design, implementation, and characterization of an automated SILAR system: validation with ZnO thin film deposition*, *Int. J. Adv. Manuf. Technol.* **123**, 1189–1201 (2022).
62. T.A. Taha, R. Saad, M. Zayed, M. Shaban, and A.M. Ahmed, *Tuning the surface morphologies of ZnO nanofilms for enhanced sensitivity and selectivity of CO₂ gas sensor*, *Appl. Phys. A Mater. Sci. Process.* **129**, 115 (2023).
63. R. Saravana Kumar, R. Sathyamoorthy, P. Matheswaran, P. Sudhagar, and Y.S. Kang, *Growth of novel ZnO nanostructures by soft chemical routes*, *J. Alloys Compd.* **506**, 351–355 (2010).
64. P. Shankar and J.B.B. Rayappan, *Room temperature ethanol sensing properties of ZnO nanorods prepared using an electrospinning technique*, *J. Mater. Chem. C* **5**, 10869–10880 (2017).
65. P.V. Raja, *Deep-Level Defects in CdZnTe and CdMnTe Detectors Identified by Photo-Induced Current Transient Spectroscopy (PICTS) and Thermally Simulated Current (TSC) Techniques*, *Tel Aviv University hal-03599211* (2022).
66. M. Yang, H. Chang, J. Chen, and X. Zhu, *Multiplier Effects of Photodetectors—Source of Gain*, *Coatings* **13**, 1088 (2023).
67. J. Teiser, M. Kruss, F. Jungmann, and G. Wurm, *A Smoking Gun for Planetesimal Formation: Charge-driven Growth into a New Size Range*, *Astrophys. J. Lett.* **908**, L22 (2021).
68. X. Wang, D. Li, Q. Zhang, T. Li, Z. Cao, and F. Wang, *Experimental Study on the Agglomeration of Oily Fine Particles by Sound Wave*, *Buildings* **13**(7), 1660 (2023).
69. Z. Pan, A. Ye, A. Dave, K. Fraser, and H. Singh, *pH-dependent sedimentation and protein interactions in ultra-high-temperature-treated sheep skim milk*, *J. Dairy Sci.* **106**, 1626–1637 (2023).
70. K. He, N. Chen, C. Wang, L. Wei, and J. Chen, *Method for Determining Crystal Grain Size by X-Ray Diffraction*, *Cryst. Res. Technol.* **53**, 1700157 (2018).
71. N. Mufti, A. Damayanti, A., Aripriharta, Arramel, A. Taufiq, and Sunaryono, *The growth of ZnO nanorods on stainless-steel foils and its application for piezoelectric nanogenerator*, *J. Phys. Conf. Ser.* **1093**, 012004 (2018).
72. L. Liu, S. Wang, W. Liu, J. Wang, B. Zhang, J. Yang, H. Liu, and Y. Li, *Supercritical hydrothermal synthesis of nano-ZnO: Effects of key parameters and reaction mechanism*, *Ceram. Int.* **49**, 31313–31324 (2023).
73. D.A. Giannakoudakis, J.A. Arcibar-Orozco, and T.J. Badosz, *Effect of GO phase in Zn(OH)₂/GO composite on the extent of photocatalytic reactive adsorption of mustard gas surrogate*, *Appl. Catal. B Environ.* **183**, 37–46 (2016).
74. A. Sakthivelu, S. Valanarasu, and J.J. Prince, *Effect of pH on SILAR deposited ZnO thin films*, *Int. J. Chem. Sci.* **7**, 2463–2469 (2009).

75. A. Moumen, B. Hartiti, E. Comini, Z. El Khalidi, H.M.M.M. Arachchige, S. Fadili, and P. Thevenin, *Preparation and characterization of nanostructured CuO thin films using spray pyrolysis technique*, Superlattices Microstruct. **127**, 2–10 (2019).
76. N.K. Das, J. Chakrabarty, S.F.U. Farhad, A.K. Sen Gupta, E.M.K. Iqbal Ahmed, K.S. Rahman, A. Wafi, A.A. Alkahtani, M.A. Matin, and N. Amin, *Effect of substrate temperature on the properties of RF sputtered CdS thin films for solar cell applications*, Results Phys. **17**, 103132 (2020).
77. N.C. Juliana, O.N. Livinus, and I.D. Chigozie, *Results of SILAR Cycles Variation on the Optical, Structural and Electrical Properties of Lead Iodide Thin Films*, Appl. Phys. **4**, 31-39 (2021).
78. T. Okuno, M. Manago, S. Kitagawa, K. Ishida, K. Kusada, and H. Kitagawa, *NMR-based gap behavior related to the quantum size effect*, Phys. Rev. B **101**, 121406(R) (2020).
79. W. Wan, C. Tang, A. Qiu, and Y. Xiang, *The size effects of point defect on the mechanical properties of monocrystalline silicon: A molecular dynamics study*, Materials **14**, 3011 (2021).
80. Y.C. Liang and C.C. Wang, *Surface crystal feature-dependent photoactivity of ZnO-ZnS composite rods: Via hydrothermal sulfidation*, RSC Adv. **8**, 5063–5070 (2018).
81. S. Kumar, A. Kandasami, R.K. Singh, S. Chatterjee, D. Kanjilal and A.K. Ghosh, *Investigations on structural and optical properties of ZnO and ZnO:Co nanoparticles under dense electronic excitations*, RSC Adv. **4**, 62123-62131 (2014).
82. A. Sharma, B.P. Singh, S. Dhar, A. Gondorf, and M. Spasova, *Effect of surface groups on the luminescence property of ZnO nanoparticles synthesized by sol-gel route*, Surf. Sci. **606**, L13–L17 (2012).
83. A. Bashir, A. Majeed, S. Naseem, and A.S. Bhatti, *Investigation of structural and optical parameters of yttrium-doped ZnO thin films prepared via spin coating of simple aqueous solution*, Bull. Mater. Sci. **44**, 95 (2021).